JACS
JOURNAL OF THE AMERICAN CHEMICAL SOCIETY
Article
pubs.acs.org/JACS

Electron Transfer in Nanoparticle Dyads Assembled on a Colloidal Template

Brittney M. Graff,[†] Brian P. Bloom,[†] Emil Wierzbinski,[†] and David H. Waldeck*[,†,‡]

[†]Department of Chemistry, University of Pittsburgh, Pittsburgh, Pennsylvania 15260, United States
[‡]Petersen Institute of Nanoscience and Engineering, University of Pittsburgh, Pittsburgh, Pennsylvania 15260, United States

Supporting Information

ABSTRACT: This work shows how to create covalently bound nanoparticle dyad assemblies on a colloidal template and studies photoinduced charge transfer in them. New results are reported for how the electron-transfer rate changes with the inter-nanoparticle distance and the energy band offset of the nanoparticles (reaction Gibbs energy). The experimental findings show that the distance dependence is consistent with an electron tunneling mechanism. The dependence of the rate on the energy band offset is found to be consistent with Marcus theory, as long as one performs a sum over final electronic states. These results indicate that our understanding of electron transfer in molecular donor−bridge−acceptor assemblies can be translated to describe nanoparticle−bridge−nanoparticle assemblies.

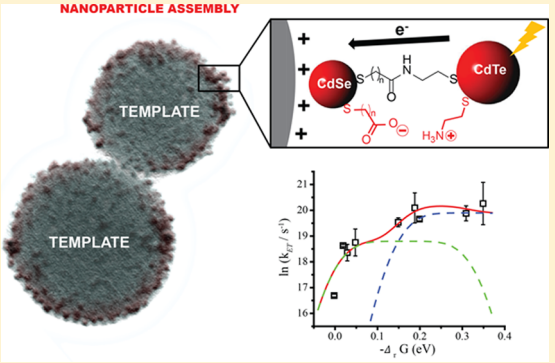

INTRODUCTION

Electron-transfer reactions are ubiquitous in nature, and their control is important for many technologies. This work explores fundamental aspects of photoinduced electron transfer between semiconductor nanoparticles, which are one promising material for use in new types of solar cells and solid-state lighting technologies.[1] In particular, bulk heterojunction solar cells are a low-cost photovoltaic technology;[2−4] however, the best bulk heterojunction solar cells currently have an efficiency of 8−10%, which is less than their predicted maximum efficiency of 15−18%.[5] Organic−inorganic nanoparticle composites offer one strategy for improving the performance of such inexpensive self-assembling photovoltaic structures but better control over the optical properties and the charge separation and recombination kinetics is required for its realization. This work develops our understanding of how to manipulate semiconductor nanoparticle properties, in particular their charge transfer and recombination kinetics, to yield efficient charge separation.

Over the past few decades, the study of electron transfer in donor−bridge−acceptor (DBA) supermolecules has provided a platform for examining fundamental features of electron transfer between molecular units.[6−9] Experimental electron-transfer studies in molecular DBA systems have allowed for the detailed and rigorous examination of the predictions made by the Marcus electron-transfer model and its extensions. These studies have elucidated the dependence of electron transfer on reaction Gibbs energy and reorganization energy, as well as their dependence on molecular and solvent structure. Through the examination of different bridging units, the importance of bridge architecture, electronic structure, and connectivity have been revealed.[10−16] This understanding has allowed for the extension of these models to examine the role of solvent polarization[17] and solvent mediated electron tunneling.[18,19] The current study introduces an analogous platform with the aim of examining electron transfer between nanoparticles; i.e., donor and acceptor molecular units are replaced by semiconductor nanoparticles. The ability to vary the optical and electronic properties of semiconductor nanoparticles by varying their size[20] provides a strategy for examining whether Marcus theory and our understanding of electron transfer in molecules can be directly translated to nanostructures or whether they need to be modified.[21,22] This work provides a novel protocol for preparing DBA nanoparticle structures and examining electron-transfer rates in them.

Charge transfer at semiconductor heterojunctions and interfaces has been studied since the middle of the 20th century, and it is well known that a staggered, or Type II, band alignment facilitates charge transfer.[23−25] The same energy level structure is important for charge transfer in semiconductor nanoparticles and a number of earlier works have demonstrated charge transfer for such nanomaterials. A recent review provides an up-to-date and comprehensive discussion for charge transfer involving nanoparticles,[26] including the importance of how donor−acceptor ratios, donor−acceptor distance, and environmental factors can affect observed electron-transfer rates. As the current study examines charge transfer in cadmium selenide/cadmium telluride (CdSe/CdTe) heterojunctions this discussion focuses on the earlier work for these materials. Scholes and co-workers have examined charge transfer in CdTe/CdSe heterostructure nanorods and core/shell nanoparticles.[27,28] They confirmed the presence of a charge-transfer band from which they were able to

Received: July 6, 2016
Published: September 16, 2016

DOI: 10.1021/jacs.6b06991
J. Am. Chem. Soc. 2016, 138, 13260−13270

quantify the reorganization energy λ and reaction Gibbs free energy $\Delta_r G$. They found a very small reorganization energy which is consistent with the nanoscale size of the donor and acceptor. Several groups have studied charge transfer in CdSe and CdTe nanoparticle aggregates that are linked together electrostatically or covalently, and charge-transfer rates in these systems range from picoseconds to nanoseconds.[29,30] It is likely that these assemblies contain a large variation in charge-transfer rates because of their distribution of sizes, interparticle distance, and band energy differences. Additionally, because the nanoparticle aggregates that have been studied do not have uniform, local donor-to-acceptor molar ratios, there can be large variations in the measured charge-transfer rate.[29,31] While nanoparticle aggregates of this sort are highly relevant for understanding charge transfer in bulk heterojunction materials, more precise assemblies are needed to understand how the structural features impact charge separation and recombination kinetics, enabling the design of better bulk heterojunction materials.

This work describes electron transport kinetics of nanoparticle assemblies, approximately nanoparticle dyads, that have a more well-defined architecture than randomly formed aggregates of nanoparticles in solution. Preparation of such assemblies was accomplished by utilization of a colloidal template and stepwise formation of a designed nanoparticle composite architecture. Figure 1 shows a general scheme for the nanoparticle assembly formation and their anticipated structure.

Covalent linkage of the nanoparticles by way of organic capping ligands on the nanoparticles provides good control over the interparticle distance and enables independent manipulation of the nanoparticle size. By studying the relationship between the electron-transfer rate and the interparticle distance, changed by variation of the number of methylene groups in an amide linker chain, we demonstrate that the natural log of the electron-transfer rate falls off linearly with the length of the interparticle bridge. By studying the electron-transfer rate as a function of the reaction driving force (Gibbs free energy, $\Delta_r G$), we demonstrate that the electron-transfer rate increases as $\Delta_r G$ becomes more negative, and this dependence can be modeled using semiclassical Marcus theory. These findings imply that our understanding of electron transfer in molecular systems can be translated to describe electron transfer in inorganic semiconductor nanoparticle systems.

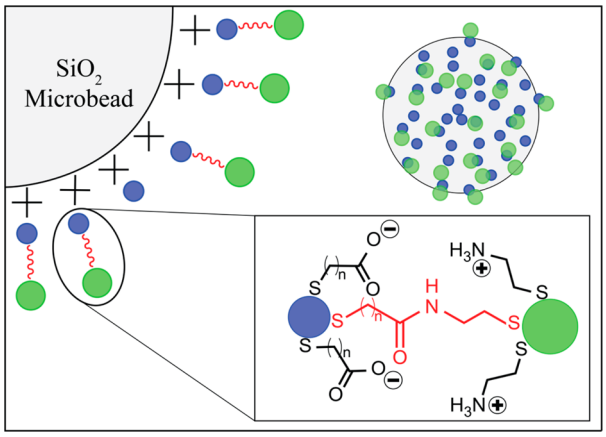

Figure 1. Cartoon describing the attachment of the nanoparticles on a microbead. The acceptor nanoparticle (blue) is electrostatically attached to a SiO_2 template and covalently linked (red) to a donor nanoparticle (green) yielding a nanoparticle dyad on the microbead (2NPA). The upper right corner of the image depicts a cartoon of a single microbead with many nanoparticles on the surface. The upper left-hand corner zooms in on one section of the microbead containing many nanoparticle dyads, and the lower right-hand corner zooms in on a single dyad. The capping ligand on the donor nanoparticles was always cysteamine, but the acceptor nanoparticles had a variety of different surface ligands. The number of methylene units, *n*, in the cartoon indicates the various ligands utilized in these experiments (n = 1, TGA; n = 3, MBA; n = 5, MHA; n = 7, MOA; n = 10, MUA). Note that in the zoomed-in image, ligand sizes are dramatically exaggerated with respect to the size of the nanoparticle.

RESULTS

Demonstration of Nanoparticle Dyad Assemblies. The formation of nanoparticle assemblies on a 500 nm diameter silicon dioxide (SiO_2) sphere has been confirmed by fluorescence, zeta potential, and electron microscopy measurements. An excess of thioglycolic acid-coated cadmium telluride nanoparticles (TGA-CdTe) were added to a solution of amine-coated SiO_2 microspheres, and it was left to shake for 1 h. After 1 h, the assembly was purified by filtration through a 100 nm porous filter; see the Supporting Information (SI) for a more detailed description of the purification protocol. The assembly is driven by the electrostatic attraction of the negatively charged nanoparticle for the positively charged microsphere.

Figure 2 shows spectral data confirming the loading of negatively charged CdTe nanoparticles onto the silica beads, i.e., one-nanoparticle assemblies (1NPA). The spectra in Figure 2A show the characteristic emission peak from the TGA-CdTe (red dashed) in solution and when it is bound onto the microbead (blue). Figure 2B shows the photoluminescence decay for the nanoparticle on the microbead (blue) and compares it to that of the nanoparticle in solution (red). Note that the fluorescence decay for the 1NPA differs from that of the free nanoparticle in solution. The electron-transfer analysis accounts for this effect (*vide infra*); its origin will be reported on elsewhere. When the nanoparticle is removed from the microsphere, however, the photoluminescence decay recovers to that obtained before bead loading (see Figure S5).

After the first nanoparticle layer was successfully assembled, a second nanoparticle could be attached to the first one, either through electrostatic interactions or by covalent bonding. These two-nanoparticle assemblies (2NPA) on the microsphere were confirmed by zeta potential (electrokinetic potential) and fluorescence energy-transfer measurements. After the addition of each oppositely charged layer, a zeta potential measurement was taken. A change in the sign of the zeta potential indicated the presence of an oppositely charged layer on the surface of the microbead. The fluorescence of the filtrate, 1NPA, and 2NPA was monitored. The decrease in the filtrate emission intensity after each successive filtration indicated that no free nanoparticle was left in solution. Additionally, the existence of an emission peak from each nanoparticle in the 2NPA was indicative of their attachment. In the studies reported herein, a positively charged cysteamine-coated CdTe (CA-CdTe) nanoparticle was covalently attached to a TGA-CdTe through the formation of an amide bond, facilitated by the catalyst 1-ethyl-3-(3-(dimethylamino)propyl)carbodiimide (EDC) and N-hydroxysulfosuccinimide (sulfo-NHS). The purification of the reaction mixture was the same as that used for the 1NPA. Throughout this series of experiments, the ratio between the donor and acceptor nanoparticles was maintained at 3 donors:4 acceptors. We refer to these assemblies as nanoparticle dyads.

DOI: 10.1021/jacs.6b06991
J. Am. Chem. Soc. 2016, 138, 13260−13270

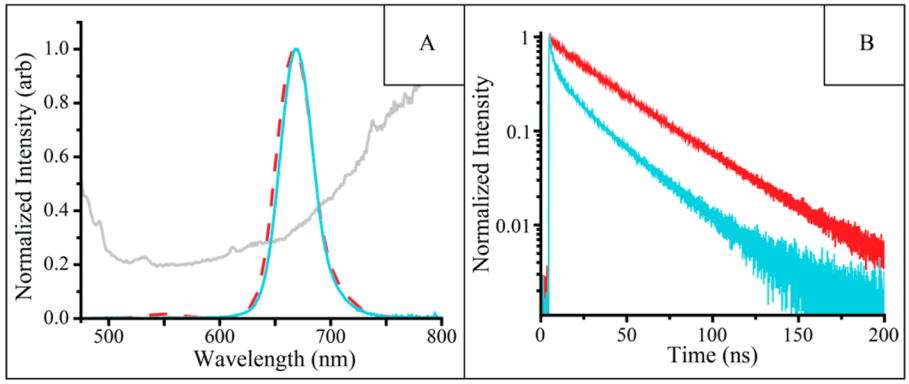

Figure 2. (A) Normalized steady-state fluorescence spectra of the TGA-CdTe in solution (red dashed) and assembled on the colloidal microspheres (1NPA) in solution (blue) (λ_{ex} = 440 nm, 0.7 × 0.7 nm resolution, 0.1 s integration time). Note that the microsphere scattering is subtracted from the 1NPA spectrum. The scattering from the microsphere (gray) is shown and is amplified by 25 times compared to that of the 1NPA spectrum. (B) Photoluminescence decays of the TGA-CdTe in solution (red) and the 1NPA (blue) in solution.

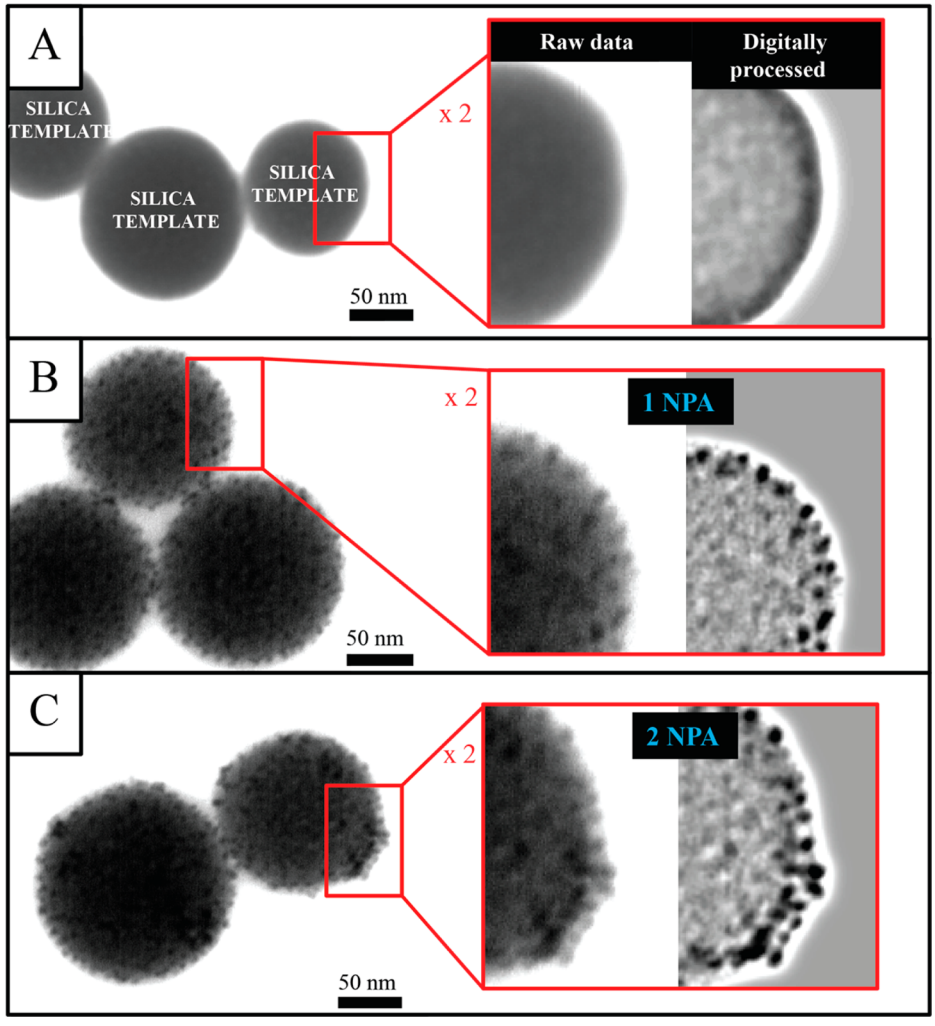

Figure 3. Electron microscopy characterization. (A) Micrograph of the silica sphere used as a template for the nanoparticle assembly. (B) Example of the 1NPA composed of CA-CdTe on silica beads. (C) Image for 2NPA assemblies obtained after further modification of the 1NPA with MPA-CdSe. Insets show digitally 2-fold magnified fragments of the original micrographs together with images processed with an FFT bandpass filter. Contrast of the features outside of the ca. 1.5−7 nm diameter range was suppressed by the bandpass filter (right panels in the insets). Note that the diameter of the silica spheres template and the size of the nanoparticles differs significantly from the parameters used in electron-transfer studies. See text for details. Additional data that confirm the fabrication of 1NPAs and 2NPAs are provided in the SI.

Formation of the 1NPA and 2NPA was further confirmed by electron microscopy. Because of instrumental limitations it was necessary to change the relative sizes of the particles in the assemblies and to increase the microbead loading so that they could be imaged; however, the chemistry and procedures were kept the same. For the images shown in Figure 3, the

DOI: 10.1021/jacs.6b06991
J. Am. Chem. Soc. 2016, 138, 13260−13270

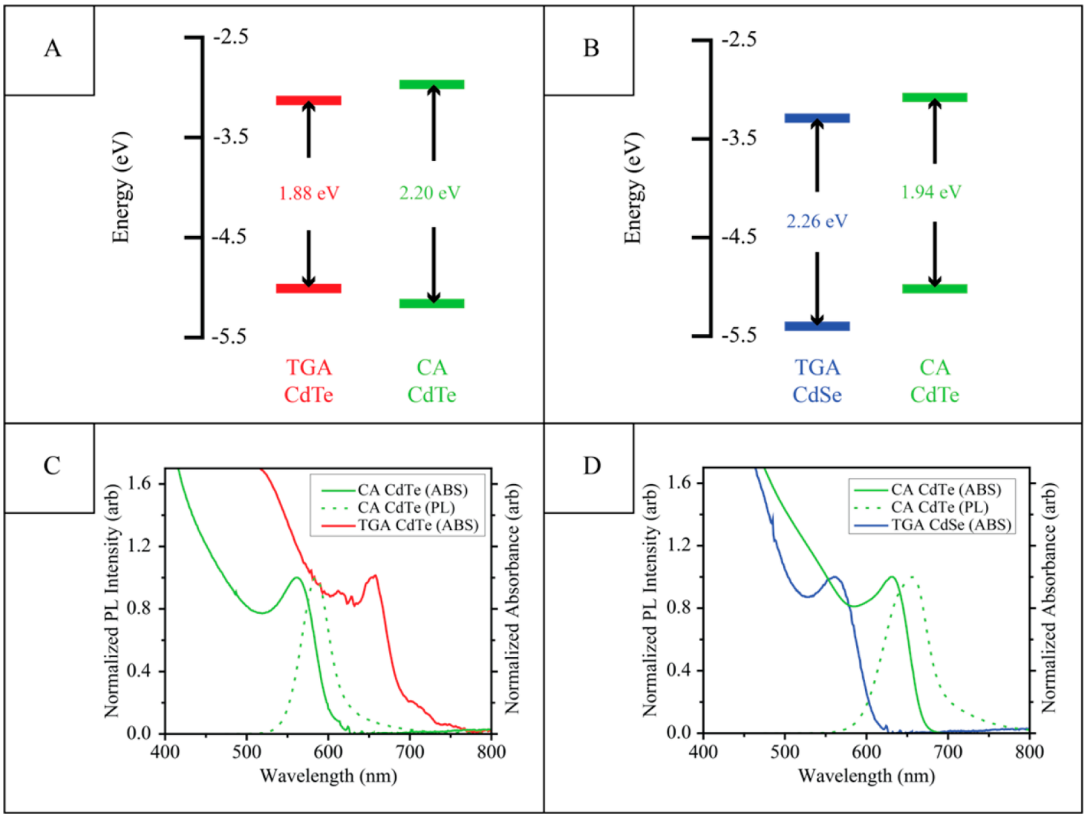

Figure 4. Energy schemes and optical spectra are shown for the nanoparticle assemblies under investigation. (A,B) Donor (green) and acceptor (red/blue) energy levels for the cases of Förster energy transfer (A) and electron transfer (B). (C,D) Normalized absorbance (solid) and photoluminescence (dashed) in the cases of Förster energy transfer (C) and electron transfer (D).

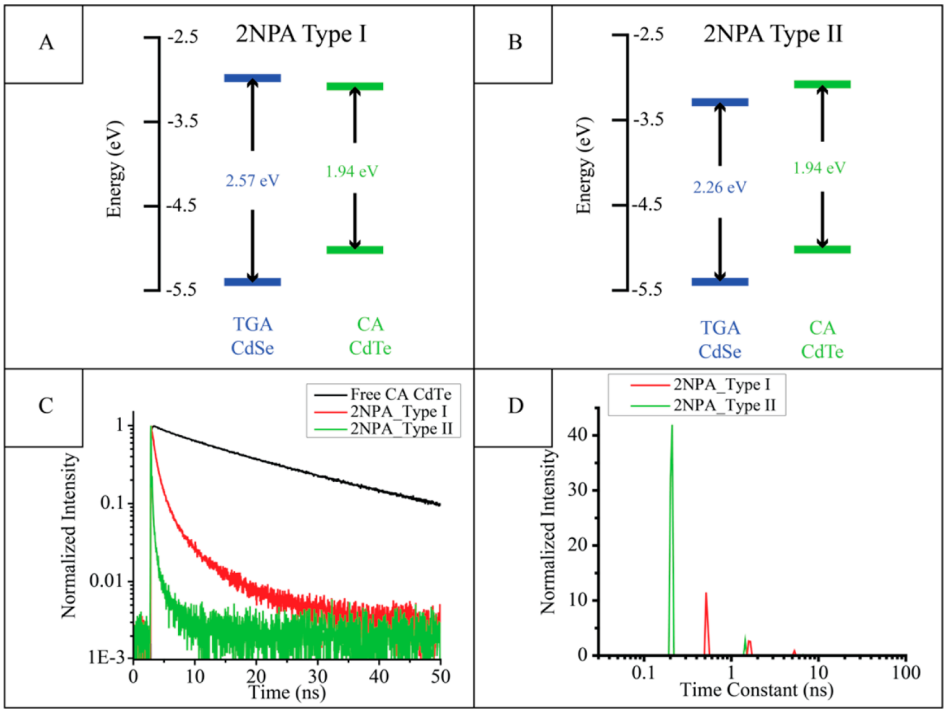

Figure 5. Band diagrams for the nanoparticle assemblies used in the electron-transfer rate measurements. In each case the smaller band gap nanoparticle, CA-CdTe, is photoexcited. (A) Band edges for the Type I reference system. (B) Band edges for the photoinduced electron transfer. (C) Photoluminescence decays and (D) lifetime distribution fitting results for the CA-CdTe free in solution (black), the Type I 2NPA (red), and the Type II 2NPA (green). The donor emission is quenched most dramatically in the Type II nanoparticle dyad assembly.

DOI: 10.1021/jacs.6b06991
J. Am. Chem. Soc. 2016, 138, 13260−13270

microspheres were approximately 150 nm; the CdSe nanoparticle was 5.5 nm, and the CdTe nanoparticle was 4.0 nm. Note that the smaller microsphere reduced charging effects in the scanning transmission electron microscopy (STEM) measurement, but it caused the filtration procedure to be less effective. Figure 3A shows an example STEM image of a colloidal silica template with a nominal diameter of 150 nm. The beads composed of the template are characterized by a spherical shape with a surface that is devoid of any distinguishable features. The 1NPAs (Figure 3B) show distinguishable features (ca. 5 nm) that are uniformly distributed on the template's surface. The dark spots in Figure 3B are assigned to the 4.0 nm CdTe nanoparticles, and they show a typical separation of several nanometers along the surface. Presumably, the nanoparticles form a sparse monolayer rather than a compact film because of their electrostatic repulsion. The 2NPA (see Figure 3C) is less evenly distributed than the 1NPA; nevertheless, a bilayer-type surface film is formed in certain parts of the template surface, rather than large aggregates of the nanoparticles. Please note that while some acceptor nanoparticles (inner layer) do not have any donor nanoparticles (outer layer) attached to them, only the donor nanoparticles are photoexcited. Details in the structures of 1NPA and 2NPA are somewhat more distinguishable on the images digitally processed with an FFT bandpass filter,[32] which improves the image contrast at the edges of the beads (see insets in Figure 3). Additional examples of STEM images of 1NPA and 2NPA and particles size analysis based on microscopy data are provided in the SI.

Mechanism of Fluorescence Quenching. The mechanism of fluorescence quenching in the nanoparticle dyads can be controlled by manipulating the energy bands of the individual nanoparticles. Figure 4A shows a Type I system which has an energy level structure that allows both charge transfer and Förster energy transfer if the wider bandgap nanoparticle is excited; the spectral overlap integral between the donor emission (green, CA-CdTe) and the acceptor absorption (red, TGA-CdTe) was maximized (Figure 4C). In contrast, if the smaller bandgap nanoparticle, TGA-CdTe, is excited, then both charge transfer and Förster energy transfer are blocked. Figure 4B shows a Type II, or staggered, energy band offset. In this case, if the wider bandgap semiconductor (TGA-CdSe) is excited, both Förster energy transfer and hole transfer to the smaller band gap nanoparticle (CA-CdTe) are allowed. In contrast, excitation of the smaller bandgap nanoparticle allows only electron transfer from the smaller bandgap CA-CdTe to the larger bandgap TGA-CdSe.

The electronic-state energies of the CdSe and CdTe nanoparticles reported in Figures 4 and 5 are inferred from previous experimental measurements. For CdSe nanoparticles functionalized with a thiol linker it was shown that the valence band maximum does not shift greatly with size.[33] The conduction band minimum was then determined by using the optical band gap and exciton binding energy of the nanoparticle.[34] For CdTe nanoparticles the valence and conduction band energies reported by Jasieniak et al.[35] were utilized. Although a different passivating ligand was used in their experiments than in the nanoparticle assemblies studied here, electrochemical measurements were performed on a 4.1 nm CA-CdTe nanoparticle, and they showed that the valence band maxima are in good agreement with Jasieniak et al.[35] (Figure S6).

Time-resolved photoluminescence (PL) measurements were used to monitor the quenching rate of the donor, CA-CdTe, for the two assemblies shown in Figure 4. In each case the fluorescence decay profiles were non-exponential but could be well characterized by a distribution of lifetime components. To ensure a self-consistent analysis the nanoparticle assemblies were also fit to a sum of exponentials. Examples of the fluorescence decay data and the fitting are provided in Figure S8. For this survey study, the fluorescence decay rate of the CA-CdTe free in aqueous solution was used as a reference system for extracting the quenching rate constants.

Two interparticle distances, obtained by changing the number of methylene groups in the capping ligand for the acceptor nanoparticle, were studied for the Type I and Type II nanoparticle assemblies (see Table 1). For the short linker, thioglycolic acid (TGA) was used; and for the long linker, mercaptoundecanoic acid (MUA) was used. For the Type I assemblies both distances were found to have a quenching rate of about 1.65×10^9 s^{-1}, and for the Type II assemblies the donor nanoparticle was quenched 9 times more strongly for the shorter interparticle distance than for the longer distance case (see Table 1). The difference in fluorescence quenching rate is consistent with the difference in distance dependences that are expected for energy transfer and electron transfer; and it substantiates the nanoparticle dyad energy band alignments of Figure 4. If one approximates the nanoparticles as dipole absorbers, the Förster energy-transfer model gives a Förster radius of 50 Å which is consistent with the weak distance dependence. Electron-transfer rates are expected to decay more rapidly than Förster energy-transfer rates as a function of distance, which indicates that the Type II heterojunction assemblies undergo electron transfer.[29]

Table 1. Dyad Assemblies (2NPA) and Corresponding Quenching Rates, k_{quench}

	Type I		Type II	
distance (Å)	6.2	12.2	6.2	12.2
k_{quench} (ns^{-1})	1.7 ± 0.1	1.6 ± 0.1	3.6 ± 0.08	0.4 ± 0.08
X	TGA	MUA	TGA	MUA

[a]Type I assemblies are Microsphere/X-CdTe/CA-CdTe and Type II assemblies are Microsphere/X-CdSe/CA-CdTe. X is the capping ligand on the acceptor QD; TGA is thioglycolic acid and MUA is mercaptoundecanoic acid. The error in k_{quench} was calculated from the width of the lifetime distribution peak; see SI for more details.

Note that the quenching rates in Table 1 overestimate the actual electron-transfer rate, because this analysis does not account for the fact that the nanoparticles experience some intrinsic quenching on the microbead assembly (see Figure 2B). In order to provide a more realistic reference system for the quantitative studies of the electron-transfer rate that are described below, a Type I system for which Förster energy transfer and electron transfer are blocked was used as the reference system (*vide infra*).

Distance-Dependent Electron-Transfer Study. The electron-transfer rate was examined as a function of the inter-nanoparticle distance by using five acceptor ligand lengths, differing by the number of methylene groups. Because the nanoparticle's proximity to the microsphere causes some quenching (Figure 2B), a Type I nanoparticle assembly, in which a larger bandgap nanoparticle replaces the electron acceptor nanoparticle, was used as a reference system (see Figure 5A). The Type I system was chosen as the reference because it maintains the same assembly structure, just with a larger bandgap (smaller in size) CdSe acceptor nanoparticle. In every case, the donor CA-CdTe has a smaller band gap so that Förster energy

DOI: 10.1021/jacs.6b06991
J. Am. Chem. Soc. 2016, 138, 13260−13270

transfer is not significant. Additionally, only the donor nanoparticle is excited to ensure that electron transfer rather than hole transfer is observed.[36] The relative conduction and valence bands for the Type I and Type II systems utilized in this distance-dependent study were calculated in a manner similar to that described above.

Figure 5 provides an example of the fluorescence decay data and the lifetime distribution analysis for the two different types of assemblies. Panel 5C shows fluorescence decays for the free donor nanoparticle in solution (black), the Type I 2NPA (red), and the Type II 2NPA (green). Comparison of the free donor in solution to the Type I system shows that the microsphere assembly introduces some quenching; however, a significant increase in the quenching of the donor occurs when the Type II acceptor is present. Figure 5D shows the lifetime distributions that are obtained by fitting the fluorescence decays of the Type I and Type II assemblies in Figure 5C. These distributions show that the long lifetime components (τ_{long}) have low amplitude and do not change significantly in shape or position between the two assemblies, but the short lifetime components change dramatically. Thus, it was assumed that the short lifetime component (τ_{short}) provides an accurate measure of the electron transfer. The electron-transfer rate was determined from the difference in the two short lifetime rate constants ($k = 1/\tau_{short}$), namely

$$k_{\text{Type II}} - k_{\text{Type I}} = k_{et} \quad (1)$$

The error in the electron-transfer rate constant has both systematic and random contributions. Systematic errors can arise from the use of the Type I reference system and the focus on the short time constant to obtain the rate. Because the Type I reference system accounts for electrostatic field effects on the photoluminescence and includes possible surface-state quenching pathways, it is most similar to the Type II system, while blocking the electron transfer from the band edge of the donor to the bands of the acceptor. Note that a dendrimer, PAMAM dendrimer G1.5 carboxylate sodium salt (Figure S11), control was also used and gives results similar to those found for the Type I TGA-CdSe system (see SI). In order to ensure that the method of analysis utilized was accurately describing the relationships reported in this study, the average lifetime of the decay was compared to the short time constant of each decay and it was found that there is a linear relationship between the short time constant and the average lifetime (see Figure S10). This indicates that while the magnitude of the electron-transfer rates may vary from the reported values the relationships that are described herein persist. The random error was estimated by using the full width at half-maximum of the short-lived lifetime components from the lifetime distribution fits and then propagating the error. For more discussion of these analyses and detailed k_{et} evaluation, see the SI.

Figure 6 shows a plot of the natural log of the electron-transfer rate constants versus the number of methylene units in the nanoparticle linker. These data show the results from multiple trials involving different batches of both donor (CA-CdTe) and acceptor (CdSe) nanoparticles as well as different nanoparticle coverages on the microsphere. Note that k_{et} does not change significantly with coverage, for the range studied. The ratio of donor to acceptor nanoparticles was kept consistent; even when the coverage of nanoparticle dyads on the surface of the microsphere was varied over a factor of 3. The data in Figure 6 are well described by a linear dependence on the number of methylene groups (n) in the ligand, namely

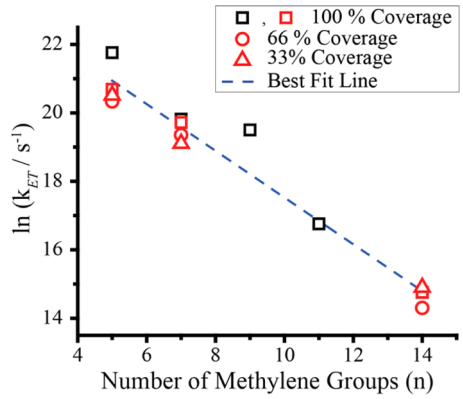

Figure 6. Natural log of the electron-transfer rate constant plotted against the number of methylene groups. The blue dashed line shows a best fit by eq 2, and it has a slope of 0.68 ± 0.04 (error determined via least-squares fitting). The black and red symbols indicate different batches of donor and acceptor nanoparticles. Various coverages for the same batch of nanoparticles were studied and are distinguished by their symbol: maximum coverage is marked with squares, two-thirds maximum coverage with circles, and one-third maximum coverage with triangles. In all cases the donor-to-acceptor ratio was maintained.

$$k_{et} = k_{et}(n = 0)\exp(-\beta n) \quad \text{or}$$
$$\ln(k_{et}) = -\beta n + \ln(k_{et}(n = 0)) \quad (2)$$

where k_{et} is the electron-transfer rate constant and β is the tunneling decay constant per methylene unit. Note that for the number of methylene groups, n, it has been assumed that all of the linkages between the donor and acceptor (from thiol to thiol) including the amide bond behave akin to a methylene group. For tunneling through a self-assembled monolayer of alkanes, workers[37,38] have reported β values ranging from 0.9 to 1.1 per methylene; however, β = 0.68 was observed in this study. Explanations for rationalizing this difference in distance dependence are described in the Discussion section.

Dependence on $\Delta_r G$. The electron-transfer rate in the nanoparticle dyad systems was studied as a function of the reaction Gibbs energy, $\Delta_r G$, by changing the size of the acceptor nanoparticle (CdSe) which changes the conduction band offsets. In all cases the interparticle distance was fixed by using cysteamine (CA) as the ligand shell for the donor nanoparticle and mercaptohexanoic acid (MHA) as the ligand shell for the acceptor nanoparticle, ~14.8 Å. Experimentally it is observed that as the reaction free energy becomes more favorable, the electron-transfer rate increases in a monotonic manner (Figure 7).

The experimental data are well described by the traditional semiclassical Marcus equation (eq 3), as long as one includes the two possible final electronic states: S_e and P_e that reside in the acceptor's conduction band. The S_e state of CdSe is taken to be the conduction band edge, and the difference in energy between the S_e and P_e states was fixed at 0.15 eV, in keeping with earlier reports.[39] While use of the S_e or P_e state alone was not able to reproduce the data (see dashed curves), summing over the first two electronic states of the acceptor was able to represent the experimental data accurately (Figure 7, red). More details on the determination of the conduction and valence bands are provided in the SI. The energy offset of these two discrete electronic states is what causes the Marcus curve to display a second rise at approximately −0.15 eV. For $\Delta_r G$ near zero the S_e state dominates, but as $\Delta_r G$ becomes more negative the P_e state

DOI: 10.1021/jacs.6b06991
J. Am. Chem. Soc. 2016, 138, 13260−13270

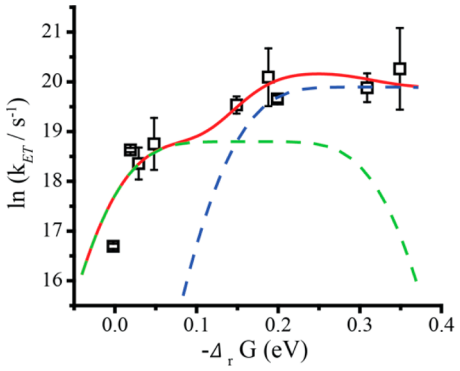

Figure 7. Natural log of the electron-transfer rate constant plotted against $-\Delta_r G$ for the experimental data (black squares). The red curve shows a fit by the semiclassical Marcus equation with a sum over electronic final states for the first two energetic states of the acceptor (solid red); the dashed lines indicate using only the first excited state (green) or the second excited state (blue). See text for details.

contributes more to the reaction rate. Equation 3 shows the explicit form of the semiclassical equation,[17]

$$k_{ET} = \frac{2\pi}{\hbar}|V|^2 \frac{1}{\sqrt{4\pi\lambda_s k_B T}} \times \left[\sum_{n=0}^{\infty} e^{-S}\left(\frac{S^n}{n!}\right) \exp\left(-\frac{(\lambda_s + \Delta_r G(S_e) + n h\nu)^2}{4\lambda_s k_B T}\right) + 3\sum_{n=0}^{\infty} e^{-S}\left(\frac{S^n}{n!}\right) \exp\left(-\frac{(\lambda_s + \Delta_r G(P_e) + n h\nu)^2}{4\lambda_s k_B T}\right)\right] \quad (3)$$

where k_B is Boltzmann's constant, $|V|$ is the electronic coupling matrix element, $\Delta_r G$ is the reaction free-energy, λ_s is the outer-sphere or solvent reorganization energy, ν is the frequency of the effective quantized vibrational mode, and S is the Huang–Rhys factor, given as the ratio of the inner-sphere reorganization energy, λ_v, to the quantized mode energy spacing, $\lambda_v/h\nu$. The $h\nu$ term refers to the energy of a single effective quantized mode associated with the electron-transfer reaction, and in this analysis it was taken to correspond to the longitudinal optical phonon frequency of the acceptor (207 cm^{-1} for CdSe).[40] The solvent reorganization energy was approximated by using a two-sphere model in a dielectric continuum, namely[17]

$$\lambda_s = \frac{e^2}{4\pi\varepsilon_0}\left(\frac{1}{D_{OP}} - \frac{1}{D_S}\right)\left(\frac{1}{2r_D} + \frac{1}{2r_A} - \frac{1}{R}\right) \quad (4)$$

where D_{OP} is the optical dielectric constant, D_S is the static dielectric constant, r_D is the donor nanoparticle radius, r_A is the acceptor nanoparticle radius (which is changing in this system), and R is the interparticle distance. The two-sphere model predicts that the value of the solvent reorganization energy, λ_s, should lie between 0.005 and 0.05 eV; the fit to the experimental data was constrained to have a λ_s over this range. In addition to λ_s, the electronic coupling parameter and the inner-sphere reorganization energy, λ_v, were floated to minimize the residuals. The best-fit curve is indicated by the red line in Figure 7. The best-fit parameters were found to be $\lambda_s = 0.029$ eV, $\lambda_v = 0.009$ eV, and $|V| = 2.7$ cm^{-1}.

Note that eq 3 assumes that the quantized vibrational mode is significantly larger than k_BT; however, this assumption is not strictly valid. A more appropriate model is available for cases in which $h\nu \approx k_BT$,[41] and it gives a similarly good fit to the data. See the Discussion and SI for more details.

DISCUSSION

Electron-Transfer Kinetics. These studies build upon the earlier work of Wu et al.,[29] which investigated electrostatically bound semiconductor nanoparticle aggregates of variable size, by studying covalently bound semiconductor nanoparticle donor–acceptor dyads. The donor nanoparticle was photoexcited at the first excitonic peak maximum (635 nm); to minimize the effect from scattering by the microspheres, the nanoparticle fluorescence was collected at the red edge of the emission spectrum. The photoluminescence decays were fit using a lifetime distribution analysis. The difference in quenching between the Type II system which promotes electron transfer and the Type I control system was used to determine the electron-transfer rate (eq 1). Comparison of the lifetime distributions shows that the dominant change in the lifetime distribution is a shift in the value of the shortest lifetime component, and it was used to calculate an electron-transfer rate (see eq 1).

The ability to use a single lifetime component to extract an electron-transfer rate differs significantly from what other groups have observed.[42−45] Frequently, electron-transfer rates are calculated as a difference between the average lifetime of a control system (where electron transfer is not favored) and the investigated system (where electron transfer is favored). However, this process provides an effective electron-transfer rate that is an average over a nanoparticle distribution that is not necessarily known or well defined. In the absence of a charge-transfer band, it has been difficult to attribute electron transfer as arising from a single time constant in these complex assemblies.[46] For example, if we mimic the type of system designed by Wu et al.[29] and fabricate covalently bound nanoparticle aggregates in solution, the fit to the experimental photoluminescence decays are significantly less clear and the electron-transfer rates are not able to be determined as previously described in this study. Figure 8 shows data from such a system in which it can be seen that the long-lived lifetime components are not fixed in shape and position in the presence of the acceptor nanoparticle. Additionally, the amplitude of the long-lived lifetime components are much larger than that which is reported in Figure 4D. Thus, the nanoparticle dyad assemblies studied here represent an advance-

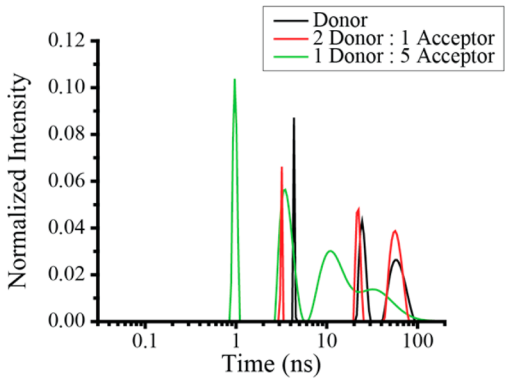

Figure 8. Sample of the PL distribution fitting for the Type II covalently bound nanoparticle assemblies. The free donor in solution, MPA CdTe (black), 2 donor:1 acceptor (red), and 1 donor:5 acceptor (green) are depicted here. The prefactors before donor and acceptor are molar ratios.

DOI: 10.1021/jacs.6b06991
J. Am. Chem. Soc. 2016, 138, 13260−13270

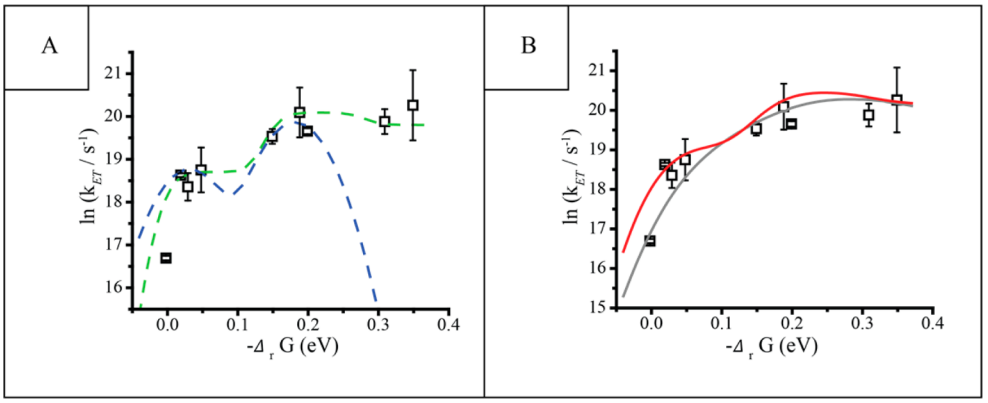

Figure 9. Natural log of the electron-transfer rate constant is plotted against the reaction Gibbs energy, $-\Delta_r G$, for the experimental data (black squares). (A) Best fits to the classical Marcus theory (blue) and a semiclassical Marcus theory at intermediate temperature ($h\nu \approx k_B T$, green). (B) Best fits to the data by the semiclassical equation (eq 3) (green curve) and by eq 3 while accounting for the size distribution in the nanoparticles (see text).

ment toward the sort of system homogeneity found in molecular dyads.

Electron-Transfer Rate as a Function of Interparticle Distance. The data in Figure 6 report how charge transfer changes with the distance between two semiconductor nanoparticles that form a dyad. Over the past two decades a number of closely related studies have been performed; other research groups have investigated how electron-transfer rates in semiconductor nanoparticles attached to either molecular/polymer[47] or metal/metal oxide[46,48] systems change as a function of donor−acceptor distance. In the metal and metal oxide systems, the semiconductor quantum dots have been linked through a molecular bridge, and electron transfer between a semiconductor quantum dot and a metal oxide[46] was studied as a function of interparticle distance, yielding a decay parameter of 0.94 per methylene. This is similar to but is somewhat larger than the β value of 0.68 per methylene found for the 2NPAs. Tagliazucchi et al.,[47] studied electron transfer between CdSe nanoparticles and poly(viologen) for varying viologen units, and found β to be 0.8 per Å, and if one assumes the length of a methylene unit is 1.26 Å,[49] then the value of β for this work is determined to be 0.54 per Å.

For traditional alkane self-assembled monolayers the distance dependence for alkane chains is reported to range from 0.9 to 1.1 per methylene.[37,38] There are a few explanations for why the distance dependence for this system would be less than the value of 1.0 per methylene. The current system has an amide linkage, and others report that amide groups can enhance the electron-transfer efficiency and yield a $\beta < 1.0$.[48,50,51] Additionally, when the molecules in a SAM are not oriented normal to the surface, both "through-bond" superexchange and "through-space" superexchange can contribute to the electron tunneling. For example, alkanethiol SAMs on indium phosphide with a 55° tilt angle were shown to have a β value of 0.49 per methylene.[38,52] In addition, it is likely that the packing of the ligands on the surface of the nanoparticles is not perfect, thus as the chain length increases the distance may not scale as 1.26 Å per methylene. Since it is unlikely that the ligands on the nanoparticle surface are entirely perpendicular to the surface or perfectly packed on the surface, the β value reported for the dyads seems reasonable.

In complex nanoscale systems, where electron transfer is studied as a function of distance, slopes that are much less than one are frequently reported.[12,53−57] Gilbert et al.[12] described molecular wires in which electrons can hop along the bridge, as well as tunnel through it, yielding smaller β values. In complex two-nanoparticle systems separated by "alkane-like" linkers, β values have been reported to be 0.08[56] and 0.13[57] per Å. For the current system, very shallow slopes are not observed, which is consistent with an electron tunneling mechanism by way of a covalent pathway of saturated C−C bonds. Lastly, we note that the magnitude of the electron-transfer rate for the shortest linker, TGA, falls within the regime of reported electron-transfer rates in the literature for dyes directly attached to a nanoparticle.[46,47,58,59]

Free Energy Dependence of the Electron Transfer. Other groups have observed an increase in electron-transfer rate with an increase in driving force, even in locations where the inverted regime is expected.[21,60−63] Figures 7 and 9 shows plots of the electron-transfer rates versus $-\Delta_r G$, as well as fits by different versions of the Marcus model. As noted earlier, $h\nu$ was fixed at 207 cm^{-1},[40] and λ_s was restricted to lie in the range of 0.005 to 0.05 eV. The longitudinal optical (LO) phonon of the acceptor, CdSe, used for the quantized mode, ν, is known to be important for the carrier relaxation in the CdSe conduction band. It is reported in the literature to be 207 cm^{-1} over the size regime studied,[40] and although it changes with nanoparticle size, the change is small, ~5 cm^{-1}, and does not affect the fit quality. An appropriate range for the solvent reorganization energy, λ_s, was chosen by using a two-sphere model.[64] In a CdSe-CdTe nanorod heterostructure reported on by Scholes et al.,[63] a charge-transfer band was present and the reorganization energy of 0.02 eV was calculated directly using the shape of the free energy curves. Thus, the best-fit value of 0.029 eV seems reasonable.

Figure 9 compares the predictions of different models for describing the experimental data for the $\Delta_r G$ trend. The classical Marcus theory (blue dashed curve, left panel), without quantized nuclear modes, fails to adequately describe the data, even with the inclusion of more than two product energy levels. The incorporation of the vibrational states (i.e., longitudinal optical phonon mode) in the semiclassical Marcus theory ($k_B T > h\nu$) helps to broaden the Marcus curve and describes the system well over the $\Delta_r G$ regime investigated (red, right panel). If we account for the fact that $h\nu \approx k_B T$, we must use a different form for the semiclassical Marcus equation (see Eqn S4 in the SI), but we obtain a similarly good fit to the data (dashed green line, left panel). The best-fit model parameters change somewhat; most notably the value of the electronic coupling is 0.3 cm^{-1} rather than 2.7 cm^{-1}. Note that the model used here to describe the charge transfer is fundamentally related to the multiphonon emission model for charge carrier trapping in deep traps of a semiconductor.[65] We note that an Auger-assisted electron-

DOI: 10.1021/jacs.6b06991
J. Am. Chem. Soc. 2016, 138, 13260−13270

transfer mechanism, which has been used to describe hole transfer in the deeply inverted Marcus regime, does not need to be invoked to generate a good fit to the data. Thus, the best fit, with the most realistic physical parameters, is found by using the semiclassical Marcus equation, (aka, multiphonon emission model), either at high or intermediate temperature, over a sum of the two final states.

These model fits predict a step, or rise, in the electron-transfer rate as the reaction free energy becomes large enough to include the second excited state, P_e; however, the experimental data do not display such a rise. Given that the nanoparticles have a distribution of sizes and have a distribution of $\Delta_r G$ values, this feature in the model is likely to be masked in the data. To illustrate this effect, Figure 9B (gray curve) shows a fit by the semiclassical model (with the same parameters as in the red curve) that is convoluted with a Gaussian-shaped nanoparticle size distribution of 0.070 eV. The 0.070 eV width of the Gaussian was estimated from the width in the absorbance spectra of the nanoparticles, and its inclusion "smears" the resolution in the model prediction, giving an excellent fit to the data. Figure S12 provides a contour plot, which shows the dependence of the fit quality on values of $|V|$ and λ_s.

In an effort to assess whether the high frequency limit or the intermediate frequency model more accurately describes the data, the value of the electronic coupling at contact between the nanoparticles was obtained by extrapolating to a zero distance, using the distance dependence from Figure 6. Two limits were considered for contact, direct contact between nanoparticle atoms, as in a core−shell material, and a disulfide bond linkage.[66] For the fit by eq 3 (red curve) we obtain a 197 meV electronic coupling for direct contact and an 80 meV electronic coupling for the disulfide linkage; in contrast, for the fit by Eqn S5 in the SI (green curve) we find $|V| = 22$ meV at direct contact and 8.7 meV for a disulfide linker. For CdSe-CdTe nanorod heterostructures Scholes et al.[64] reportet 50 meV, for CdTe−CdTe aggregates (via a quantum mechanical calculation) a value of 40 meV[67] is reported, and for dye molecules directly bound to a semiconductor nanoparticle electronic couplings in the range of 10−10^3 meV have been reported. Although both models give reasonable coupling strengths, the intermediate frequency limit is more consistent with the known phonon properties of the nanoparticle.

CONCLUSIONS

A controlled covalently linked nanoparticle dyad system on a template was fabricated. The band edges of the nanoparticles in these systems were designed in a manner such that electron transfer could be studied as a function of interparticle distance and driving force. The electron-transfer rate between the nanoparticles changed exponentially with distance and the electron tunneling decay length for a hydrocarbon bridge is similar to that found for molecular dyads and for molecules tethered to an electrode surface. The semiclassical Marcus theory was able to accurately describe the relationship between electron transfer and $\Delta_r G$, as long as one performs a sum over the manifold of final states. Important differences between the nanoparticle dyads and molecular dyads arise from the small reorganization energies in the nanoparticles (because of their size and rigidity) and the ability to tune the free energy difference by changing the nanoparticle size. These findings imply that much of the knowledge gained from studies in molecular systems can be readily translated to the case of nanoparticle quantum dots and should prove useful for understanding, controlling, and designing bulk heterojunction solar cells that transfer charge using semiconductor nanoparticles.

EXPERIMENTAL DETAILS

Selenium powder (99.999%), tellurium powder (99.999%), cadmium chloride ($CdCl_2$, 99%) sodium borohydride ($NaBH_4$, 98%), CdO (99.999%), thioglycolic acid (TGA), 4-mercaptobutyric acid (MBA), 6-mercaptohexanoic acid (MHA), 8-mercaptooctanoic acid (MOA), 11-mercaptoundecanoic acid (MUA), 1-ethyl-3-(3-(dimethylamino)-propyl)carbodiimide (EDC), *N*-hydroxysulfosuccinimide (S-NHS), phosphate-buffered saline (PBS) tablets, oleic acid (OA), and trioctylphosphine oxide (99%) were purchased from Sigma-Aldrich. Trioctylphosphine was purchased from Strem Chemicals. Octadecylphosphonic acid (ODPA, >99%) and tetradecylphosphonic acid (TDPA, >99%) were purchased from PCI Synthesis. Silica microbeads, both amine-coated and bare, 150 and 500 nm diameter, were purchased from Polysciences, Inc. All reagents and solvents were used as received. Water used in all experiments was purified by a Barnstead Nanopure system, and its resistance was 18.2 MΩ-cm at 25 °C.

Carboxylic Acid-Terminated Cadmium Selenide (CdSe). ODPA-CdSe nanoparticles, <2.5 nm, as well as OA-CdSe nanoparticles, >2.5 nm, were synthesized following previously published methodologies.[68,69] The purified nanoparticles were ligand exchanged to TGA, MBA, MHA, MOA, or MUA by stirring the ligand in a solution whose concentration was 1000 times in excess to that of the nanoparticle. The mixture was stirred overnight in 4.0 mL of a 50% water (pH = 11)/50% chloroform solution. The exchanged nanoparticles were then isolated from the water phase and purified through syringe and centrifugal filtration. For synthesis of larger, 5.5 nm, OA CdSe nanoparticles a multiple injection of the selenium precursor was utilized.

Amine-Terminated CdSe. ODPA-CdSe, 2.2 nm, and OA-CdSe, 3.1 nm, stock solutions were ligand exchanged to cysteamine (CA) through a precipitation process, demonstrated previously by Strekal et al. for CdSe/ZnS core−shell nanoparticles.[70] The precipitation was performed through the addition of 200 μL of a 20 mg/mL concentration CA/methanol solution to a 2.0 mL NP stock solution. The nanoparticle solutions were isolated through centrifugation and dried. The nanoparticles could then be dissolved in water and purified through syringe and centrifugal filtration

Amine-Terminated Cadmium Telluride (CdTe). CA-CdTe nanoparticles, 3.3, 4.0, and 4.1 nm were synthesized by an adaptation of a procedure by Wang et al.[71] Briefly, 1.145 g of $CdCl_2$ and 0.8521 g of CA were dissolved in 20.0 mL of water, and the pH was adjusted to be approximately 5.75. This solution was then heated to 90.0 °C and deoxygenated for approximately 20 min. Reduced tellurium was made by dissolving 127.5 mg of Te and 94.5 mg of $NaBH_4$ in 5.0 mL of water and heated under argon to 70.0 °C. The reduced tellurium precursor (2.5 mL) was injected into the cadmium solution and refluxed until the desired size was reached. The nanoparticles were purified through syringe and centrifugal filtration.

Carboxylic Acid-Terminated CdTe. Carboxylic acid-terminated CdTe nanoparticles, 4.1 and 4.4 nm, were synthesized through a two part process. First, large tetradecylphosphonic acid (TDPA)-capped CdTe nanoparticles were synthesized following a multiple injection approach using the synthesis developed by Peng et al.[72] Next, the TDPA-CdTe nanoparticles were ligand exchanged to either TGA or MUA following a procedure similar to that published by Wang et al.[36] A 10.0 mL solution of water containing 0.1 mmol $CdCl_2$ and 0.2 mmol TGA or MUA at pH 11.5 was degassed with argon at 80 °C for 10 min. Then, 0.5 mL of the TDPA-CdTe nanoparticle chloroform solution was injected and. the heating was continued until all the chloroform was boiled off. The solution was then brought to 100 °C and refluxed for 3 h. The resulting solution was purified by centrifugation and syringe filters to remove any non-soluble nanoparticles and unreacted precursors.

Assembly Formation. Nanoparticle dyads were formed by templating on a SiO_2 microsphere. The first step in a one-nanoparticle assembly (1NPA) was to attach a nanoparticle to an amine-coated SiO_2 microsphere, approximately 500 nm in diameter. Approximately 30 mg of SiO_2 microspheres (zeta potential = 41.91 ± 0.60 mV) was dispersed

DOI: 10.1021/jacs.6b06991
J. Am. Chem. Soc. 2016, 138, 13260−13270

in 1 mL of water. An excess of oppositely charged (carboxylic acid-terminated) nanoparticles was added to the microsphere solution and the total volume was adjusted to equal 3 mL. Then, it was shaken for 1 h. During this process, nanoparticles bind electrostatically to the surface of the microsphere. The assembly was purified using a stirred ultrafiltration cell with a 100 nm pore size cellulose nitrate membrane filter (Whatman). The "free" nanoparticles (<5 nm) go through the filter, but those that are attached to the SiO_2 template do not and are captured by the filter. The pressure used in the filtration was 50 psi and filtrate samples were collected. After filtration, the solid on the filter paper was suspended in 4 mL of water. An additional two to three rounds of filtrations were performed on this sample and the 1NPA was suspended in 3 mL of water. The zeta potential for a sample 1NPA was −19.66 ± 2.49 mV.

The nanoparticle dyads (2NPA) were assembled by forming an amide bond between the exposed carboxylic acid group of the 1NPA and the solvent exposed terminus of an amine-terminated nanoparticle (Figure 1). The catalyst 1-ethyl-3-(3-(dimethylamino)propyl)-carbodiimide (EDC) sulfo-NHS was used to promote this reaction. By choosing the second nanoparticle to be larger than that in the 1NPA the reaction is biased to create dyads. The 1NPA and EDC were added to a 500 mM PBS buffer solution in a 1:1000 ratio,[73] and stirred for 15 min. Then the amine-terminated nanoparticles were added to the solution and it was stirred overnight. The sample was cooled to 4 °C to quench the excess EDC and then purified using the same methodology as described above for the 1NPA. The zeta potential for a resulting 2NPA was 9.35 ± 1.45 mV. A more detailed description of this procedure can be found in the SI.

Steady-State Spectroscopy. Steady-state absorption spectra were measured on an Agilent 8453 spectrometer, and the steady-state emission spectra were measured on a Horiba J-Y Fluoromax 3 fluorescence spectrophotometer.

Time-Dependent Fluorescence Spectroscopy. Time-resolved fluorescence measurements of the nanoparticle assemblies were measured using the time-correlated single photon counting (TSCPC) technique with a PicoHarp 300 TCSPC module (PicoQuant GmbH).[74] The samples were excited at 635 nm using a synchronously pumped dye laser. All measurements were made at the magic angle. Measurements were collected using a 1 MHz repetition rate, 32 ps resolution, until a maximum count of 10 000 was observed at the peak channel. The instrument response function was measured using colloidal $BaSO_4$ and in every case the instrument response function had a full-width-at-half-maximum of ≤96 ps. The decay curves were fit to a distribution of lifetime components by a convolution and compare method using Edinburgh Instruments fluorescence analysis software technology (FAST),[75,76] namely

$$I(t) = \int_{\tau=0}^{\infty} \alpha(\tau) \exp(-t/\tau)\, d\tau \quad (5)$$

Zeta Potential Measurements. Zeta potential measurements were performed at room temperature in a 90° geometry with a 532 nm laser (Brookhaven Instrument Co.). The electrophoretic mobility measurements were performed on the same instrument at room temperature with an electrical field strength of 16 V/cm and a field frequency of 2.00 Hz by using a Zeta Plus zeta potential analyzer.

Scanning Transmission Electron Microscopy. Samples for electron microscopy characterization were drop casted on a carbon film on a copper transmission microscopy grid (Ted Pella Inc.). The measurements were performed using a ZEISS Sigma 500 VP Scanning Electron Microscope equipped with a STEM detector. The images were collected in bright field mode, with an electron beam acceleration voltage of 24−28 kV, 10 μm aperture, and working distance of about 2.5 mm.

■ ASSOCIATED CONTENT

Supporting Information

The Supporting Information is available free of charge on the ACS Publications website at DOI: 10.1021/jacs.6b06991.

Assembly formation details for 1NPA and 2NPA assemblies; sample electrochemistry; quenching effects as a result of the presence of catalysts; fluorescence decays and distribution fitting of energy- and electron-transfer assemblies; calculated FRET efficiency; fitting protocol details; conduction band edge (S_e) and P_e state determination; details describing the fitting to the semiclassical Marcus equation; and control studies to confirm covalently bound nanoparticle aggregates, including Figures S1−S13, Table S1, and Eqns S1−S5 (PDF)

■ AUTHOR INFORMATION

Corresponding Author

*dave@pitt.edu

Notes

The authors declare no competing financial interest.

■ ACKNOWLEDGMENTS

This work was funded by the U.S. Department of Energy (Grant No. ER46430). B.P.B. is grateful for additional financial support from the R.K. Mellon foundation.

■ REFERENCES

(1) Shami, S. *Int. J. Sci. Technol. Res.* **2015**, *4*, 165.
(2) Yu, G.; Gao, J.; Hummelen, J. C.; Wudl, F.; Heeger, A. J. *Science* **1995**, *270*, 1789−1791.
(3) Huynh, W. U.; Dittmer, J. K.; Alivisatos, A. P. *Science* **2002**, *295*, 2425−2427.
(4) Park, S. H.; Roy, A.; Beaupré, S.; Cho, S.; Coates, N.; Moon, J. S.; Moses, D.; Leclerc, M.; Lee, K.; Heeger, A. *Nat. Photonics* **2009**, *3*, 297−302.
(5) You, J.; Dou, L.; Yoshimura, K.; Kato, T.; Ohya, K.; Moriarty, T.; Emery, K.; Chen, C.; Gao, J.; Li, G.; Yang, Y. *Nat. Commun.* **2013**, *4*, 1446.
(6) Marcus, R. A.; Sutin, N. *Biochim. Biophys. Acta, Rev. Bioenerg.* **1985**, *811*, 265−322.
(7) Sanders, A. M.; Magnanelli, T. J.; Bragg, A. E.; Tovar, D. J. *J. Am. Chem. Soc.* **2016**, *138*, 3362−3370.
(8) Chen, P.; Meyer, T. J. *Chem. Rev.* **1998**, *98*, 1439−1478.
(9) Jortner, J; Bixon, M. *Electron Transfer—From Isolated Molecules to Biomolecules*; John Wiley & Sons, Inc.: New York, 1999; Parts 1 and 2.
(10) (a) Paddon-Row, M. N. *Adv. Phys. Org. Chem.* **2003**, *38*, 1−85. (b) Oevering, H.; Paddon-Row, M. N.; Heppener, M.; Oliver, A. M.; Cotsaris, E.; Verhoeven, J. W.; Hush, N. S. *J. Am. Chem. Soc.* **1987**, *109*, 3258−3269.
(11) Lawson, J. M.; Paddon-Row, M. N.; Schuddeboom, W.; Warman, J. M.; Clayton, A. H. A.; Ghiggino, K. P. *J. Phys. Chem.* **1993**, *97*, 13099−13106.
(12) Gilbert, M.; Albinsson, B. *Chem. Soc. Rev.* **2015**, *44*, 845−886.
(13) Bixon, M.; Jortner, J. *J. Chem. Phys.* **1997**, *107*, 5154−5170.
(14) Natali, M.; Campagna, S.; Scandola, F. *Chem. Soc. Rev.* **2014**, *43*, 4005−4018.
(15) Weiss, E. A.; Wasielewski, M. R.; Ratner, M. A. *Top. Curr. Chem.* **2005**, *257*, 103−133.
(16) Gu, Y.; Kumar, K.; Lin, Z.; Read, I.; Zimmt, M. B.; Waldeck, D. H. *J. Photochem. Photobiol., A* **1997**, *105*, 189−196.
(17) Liu, M.; Waldeck, D. H.; Oliver, A. M.; Head, N. J.; Paddon-Row, M. N. *J. Am. Chem. Soc.* **2004**, *126*, 10778−10786.
(18) Chakrabarti, S.; Parker, M. F. L.; Morgan, C. W.; Schafmeister, C. E.; Waldeck, D. H. *J. Am. Chem. Soc.* **2009**, *131*, 2044−2045.
(19) Zimmt, M. B.; Waldeck, D. H. *J. Phys. Chem. A* **2003**, *107*, 3580−3597.
(20) Smith, A. M.; Nie, S. *Acc. Chem. Res.* **2010**, *43*, 190−200.
(21) Zhu, H.; Yang, Y.; Hyeon-Deuk, K.; Califano, M.; Song, N.; Wang, Y.; Zhang, W.; Prezhdo, O. V.; Lian, T. *Nano Lett.* **2014**, *14*, 1263−1263−1269.

DOI: 10.1021/jacs.6b06991
J. Am. Chem. Soc. 2016, 138, 13260−13270

(22) Olshansky, J. H.; Ding, T. X.; Lee, Y. V.; Leone, S. R.; Alivisatos, A. P. *J. Am. Chem. Soc.* **2015**, *137*, 15567−15575.
(23) Sze, S. M.; Kwok, N. K. *Physics of Semiconductor Devices—Nanomaterials*, 2nd ed.; John Wiley & Sons Inc.: Hoboken, NJ, 2007.
(24) Komsa, H.; Krasheninnikov, A. *Phys. Rev. B: Condens. Matter Mater. Phys.* **2013**, *88*, 085318.
(25) Kang, J.; Tongay, S.; Zhou, J.; Li, J.; Wu, J. *Appl. Phys. Lett.* **2013**, *102*, 012111.
(26) Vokhmintcev, K. V.; Samokhvalov, P. S.; Nabiev, I. *Nano Today* **2016**, *11*, 189−211.
(27) Chuang, C.-H.; Doane, T. L.; Lo, S. S.; Scholes, G. D.; Burda, C. *ACS Nano* **2011**, *5*, 6016.
(28) (a) Scholes, G. D. *Adv. Funct. Mater.* **2008**, *18*, 1157−1172. (b) Lo, S. S.; Mirkovic, T.; Chuang, C.-H.; Burda, C.; Scholes, G. D. *Adv. Mater.* **2011**, *23*, 180−197.
(29) Wu, M.; Mukherjee, P.; Lamont, D. N.; Waldeck, D. H. *J. Phys. Chem. C* **2010**, *114*, 5751−5759.
(30) (a) Sellers, D. G.; Button, A. A.; Nasca, J. N.; Wolfe, G. E.; Chauhan, S.; Watson, D. F. *J. Phys. Chem. C* **2015**, *119*, 27737−27748. (b) Gross, D.; Susha, A. S.; Klar, T. A.; Da Como, E.; Rogach, A. L.; Feldmann, J. *Nano Lett.* **2008**, *8*, 1482−1485.
(31) Wang, D.; Zhao, H.; Wu, N.; El Khakani, M. A.; Ma, D. *J. Phys. Chem. Lett.* **2010**, *1*, 1030−1035.
(32) Rasband, W. S. *ImageJ*; U.S. National Institutes of Health: Bethesda, MD, 1997−2016; http://imagej.nih.gov/ij/.
(33) Bloom, B. P.; Zhao, L.-B.; Wang, Y.; Waldeck, D. H.; Liu, R.; Zhang, P.; Beratan, D. N. *J. Phys. Chem. C* **2013**, *117*, 22401−22411.
(34) Meulenberg, R. W.; Lee, J. I. R.; Wolcott, A.; Zhang, J. Z.; Terminello, L. J.; van Buuren, T. *ACS Nano* **2009**, *3*, 325−330.
(35) Jasieniak, J.; Califano, M.; Watkins, S. E. *ACS Nano* **2011**, *5*, 5888−5902.
(36) Wang, Y.; Liu, K.; Mukherjee, P.; Hines, D. A.; Santra, P.; Shen, H. Y.; Kamat, P.; Waldeck, D. H. *Phys. Chem. Chem. Phys.* **2014**, *16*, 5066−5070.
(37) Smalley, J. F.; Feldberg, S. W.; Chidsey, C. E. D.; Linford, M. R.; Newton, M. D.; Liu, Y.-P. *J. Phys. Chem.* **1995**, *99*, 13141−13149.
(38) Slowinski, K.; Chamberlain, R. V.; Miller, C. J.; Majda, M. *J. Am. Chem. Soc.* **1997**, *119*, 11910−11919.
(39) Norris, D. J.; Bawendi, M. G. *Phys. Rev. B: Condens. Matter Mater. Phys.* **1996**, *53*, 16338−16346.
(40) Lin, C.; Gong, K.; Kelley, D. F.; Kelley, A. M. *ACS Nano* **2015**, *9*, 8131−8141.
(41) Jortner, J. *J. Chem. Phys.* **1976**, *64*, 4860−4867.
(42) Robel, I.; Kuno, M.; Kamat, P. V. *J. Am. Chem. Soc.* **2007**, *129*, 4136−4137.
(43) Yang, J.; Oshima, T.; Yindeesuk, W.; Pan, Z.; Zhong, X.; Shen, Q. *J. Mater. Chem. A* **2014**, *2*, 20882−20888.
(44) Xu, Z.; Cotlet, M. *Angew. Chem., Int. Ed.* **2011**, *50*, 6079−6083.
(45) Dibbell, R. S.; Watson, D. F. *J. Phys. Chem. C* **2009**, *113*, 3139−3149.
(46) Morris-Cohen, A. J.; Frederick, M. T.; Cass, L. C.; Weiss, E. A. *J. Am. Chem. Soc.* **2011**, *133*, 10146−10154.
(47) Tagliazucchi, M.; Tice, D. B.; Sweeney, C. M.; Morris-Cohen, A. J.; Weiss, E. A. *ACS Nano* **2011**, *5*, 9907−9917.
(48) Wang, H.; McNellis, E. R.; Kinge, S.; Bonn, M.; Canovas, E. *Nano Lett.* **2013**, *13*, 5311−5315.
(49) Wasserman, S. R.; Tao, Y.-T.; Whitesides, G. M. *Langmuir* **1989**, *5*, 1074−1087.
(50) (a) Slowinski, K.; Majda, M. *J. Electroanal. Chem.* **2000**, *491*, 139−147. (b) Sek, S.; Misicka, A.; Bilewicz, R. *J. Phys. Chem. B* **2000**, *104*, 5399−5402. (c) Sek, S.; Palys, B.; Bilewicz, R. *J. Phys. Chem. B* **2002**, *106*, 5907−5914. (d) Slowinski, K.; Fong, H. K. Y.; Majda, M. *J. Am. Chem. Soc.* **1999**, *121*, 7257−7261.
(51) Kai, M.; Takeda, K.; Morita, T.; Kimura, S. *J. Pept. Sci.* **2008**, *14*, 192−202.
(52) Yamamoto, H.; Waldeck, D. H. *J. Phys. Chem. B* **2002**, *106*, 7469−7473.
(53) Bradbury, C. R.; Zhao, J.; Fermin, D. J. *J. Phys. Chem. C* **2008**, *112*, 10153−10160.
(54) Shein, J. B.; Lai, L. M. H.; Eggers, P. K.; Paddon-Row, M. N.; Gooding, J. J. *Langmuir* **2009**, *25*, 11121−11128.
(55) Gotesman, G.; Guliamov, R.; Naaman, R. *Beilstein J. Nanotechnol.* **2012**, *3*, 629−636.
(56) Hines, D. A.; Forrest, R. P.; Corcelli, S. A.; Kamat, P. V. *J. Phys. Chem. B* **2015**, *119*, 7439−7446.
(57) Ji, X.; Wang, W.; Mattoussi, H. *Phys. Chem. Chem. Phys.* **2015**, *17*, 10108−10117.
(58) Huang, J.; Huang, Z.; Yang, Y.; Zhu, H.; Lian, T. *J. Am. Chem. Soc.* **2010**, *132*, 4858−4864.
(59) Huang, J.; Stockwell, D.; Huang, Z.; Mohler, D.; Lian, T. *J. Am. Chem. Soc.* **2008**, *130*, 5632−5633.
(60) Chakrapani, V.; Tvrdy, K.; Kamat, P. V. *J. Am. Chem. Soc.* **2010**, *132*, 1228−1229.
(61) Sellers, D. G.; Watson, D. F. *J. Phys. Chem. C* **2012**, *116*, 19215−19225.
(62) Hyeon-Deuk, K.; Kim, J.; Prezhdo, O. V. *J. Phys. Chem. Lett.* **2015**, *6*, 244−249.
(63) Olshansky, J. H.; Ding, T. X.; Lee, Y. V.; Leone, S. R.; Alivisatos, A. P. *J. Am. Chem. Soc.* **2015**, *137*, 15567−15575.
(64) Scholes, G. D.; Jones, M.; Kumar, S. *J. Phys. Chem. C* **2007**, *111*, 13777−13785.
(65) (a) Krasikov, D. N.; Scherbinin, A. V.; Knizhnik, A. A.; Vasiliev, A. N.; Potapkin, B. V.; Sommerer, T. J. *J. Appl. Phys.* **2016**, *119*, 085706. (b) Henry, C. H.; Lang, D. V. *Phys. Rev. B* **1977**, *15*, 989.
(66) (a) Boles, M. A.; Ling, D.; Hyeon, T.; Talapin, D. V. *Nat. Mater.* **2016**, *15*, 141−356. (b) Dubois, L. H.; Nuzzo, R. G. *Annu. Rev. Phys. Chem.* **1992**, *43*, 437−463.
(67) Koole, R.; Liljeroth, P.; Donega, C. d. M.; Vanmaekelbergh, D.; Meijerink, A. *J. Am. Chem. Soc.* **2006**, *128*, 10436−10441.
(68) Kalyuzhny, G.; Murray, R. W. *J. Phys. Chem. B* **2005**, *109*, 7012−7021.
(69) Yu, W. W.; Peng, X. *Angew. Chem., Int. Ed.* **2002**, *41*, 2368−2371.
(70) Strekal, N.; Kulakovich, O.; Belyaev, A.; Stsiapura, V.; Maskevich, S. *Opt. Spectrosc.* **2008**, *104*, 50−56.
(71) Wang, R.; Wang, Y.; Feng, Q.; Zhou, L.; Gong, F.; Lan, Y. *Mater. Lett.* **2012**, *66*, 261−263.
(72) Yu, W. W.; Wang, Y. A.; Peng, X. *Chem. Mater.* **2003**, *15*, 4300−4308.
(73) Hoppe, K.; Geidel, E.; Weller, H.; Eychmuller, A. *Phys. Chem. Chem. Phys.* **2002**, *4*, 1704−1706.
(74) Yin, X.; Kong, J.; De Leon, A.; Li, Y.; Ma, Z.; Wierzbinski, E.; Achim, C.; Waldeck, D. H. *J. Phys. Chem. B* **2014**, *118*, 9037−9047.
(75) McGuinness, C. D.; Nishimura, M. K. Y.; Keszenman-Pereyra, D.; Dickinson, P.; Campbell, C. J.; Bachmann, T. T.; Ghazal, P.; Crain, J. *Mol. BioSyst.* **2010**, *6*, 386−390.
(76) Lakowicz, J. R. *Principles of Fluorescence Spectroscopy*, 3rd ed.; Springer: New York, 2006; pp 1−61, 97−155, 331−382, 443−475.

DOI: 10.1021/jacs.6b06991
J. Am. Chem. Soc. 2016, 138, 13260−13270